Synthesis of GO/TiO$_2$/Bi$_2$WO$_6$ nanocomposites with enhanced visible light photocatalytic degradation of ethylene

Ning Lv[a], Yingying Li[a], Zhuolin Huang[a], Ting Li[a], Shengying Ye[a], Dionysios D. Dionysiou[b,*], Xianliang Song[a,*]

[a] College of Food Science, South China Agricultural University, Guangzhou, 510642, PR China
[b] Environmental Engineering and Science Program, Department of Chemical and Environmental Engineering (ChEE), University of Cincinnati, Cincinnati, OH, 45221-0012, United States

ABSTRACT

A series of GO/TiO$_2$/Bi$_2$WO$_6$ (GTB) nanocomposite photocatalysts were synthesized by one-step solvothermal method. Their structures were characterized by X-ray diffractometry, Raman spectroscopy, scanning electron microscopy, X-ray photoelectron spectroscopy, UV-vis spectroscopy and photoluminescence spectroscopy. The photocatalytic activity of GTB was found to be high as investigated by the degradation of ethylene under visible light. At 0.75% GO, the degradation rate of GTB to ethylene was the highest, at 5.7 times, 2.8 times and 1.3 times that of pure TiO$_2$, Bi$_2$WO$_6$ and TiO$_2$/Bi$_2$WO$_6$, respectively. The structural characterization shows that GO and TiO$_2$/Bi$_2$WO$_6$ combine to form multiple heterojunctions, which make the forbidden bandwidth smaller. The addition of GO reduces the average grain size of GTB size, and creates an interfacial interaction with TiO$_2$/Bi$_2$WO$_6$, which inhibits the recombination of photogenerated electron-hole pairs and increases the photocatalytic activity. The GTB exhibited good stability and reusability in experiments dealing with performance evaluation during catalyst reuse.

1. Introduction

After harvesting, vegetables can continue to produce ethylene through respiratory metabolism. Ethylene is also termed a plant-ripening hormone. When the ethylene concentration exceeds the threshold concentration of fruits and vegetables (0.5 to 1 mg/m^3), the fruit and vegetable ripeness and aging is accelerated, which results in a deterioration of quality and a reduction in storage quality and shelf life of fruits and vegetables [1]. According to statistics, the annual loss of fresh fruit by ethylene damage is 30%, and vegetable losses reach as high as 40%–50%, which causes huge economic losses [2]. Therefore, a reduction or removal of ethylene during storage of fruits and vegetables is a key problem to be solved in the field of preservation. Photocatalytic oxidation represented by TiO$_2$ nanoparticles has been studied widely by many scholars [3–5]. This technology has characteristics of low cost, low energy consumption, and no pollution [6,7]. TiO$_2$ has stable chemical properties, is safe and non-toxic and has a high photocatalytic activity and low cost. It is considered to be the most promising photocatalyst for development and application, and has been examined in numerous laboratory studies as well as in few pilot-scale/larger scale studies for potential application in wastewater-treatment and antibacterial function [8,9]. However, nano-TiO$_2$ responds only to ultraviolet light because of its wide energy band gap. Most photogenerated electrons and holes recombine, which reduces photocatalytic efficiency and limits practical application. In order to enhance its photocatalytic efficiency, TiO$_2$ has been modified by precious-metal deposition [10], metallic-ion doping [11], semiconductor-compound doping [12], surface sensitization [13], and large-surface material loading [14]. Coupling of narrow-band gap semiconductors (Bi$_2$S$_3$, CdS, Fe$_2$O$_3$, Bi$_2$WO$_6$) with TiO$_2$ can broaden spectral response of composite catalysts to the visible-light region and improve the separation efficiency of electron-hole pairs. Bi$_2$WO$_6$ is one of the simplest Aurivillius-type oxides with high stability and visible-light catalytic activity. It can be coupled with TiO$_2$ to enhance charge transfer and to improve the photocatalytic activity. Many reports exist on the coupling of TiO$_2$ and Bi$_2$WO$_6$, and the higher photocatalytic activity of the composite photocatalyst than pure Bi$_2$WO$_6$ or TiO$_2$ [15,16]. But, the separation efficiency of the electron-hole pairs is limited by poor carrier transport properties. Therefore, the rational design of multi-component TiO$_2$-based composite photocatalysts and optimization of multi-channel charge separation are important for synergistic enhancement of photocatalytic activity.

---

* Corresponding authors.
  E-mail addresses: dionysios.d.dionysiou@uc.edu (D.D. Dionysiou), songxlscau@scau.edu.cn (X. Song).

Graphene oxide (GO) is an oxidation product of graphene. Its structure is similar to graphene. GO has a plane-like, two-dimensional network structure. Its surface consists of a variety of oxygen-containing groups, such as $-OH$, $C=O$, $C–OH$ and $C-COOH$, which make it more active than graphene. GO's special monoatomic layer structure gives it unique physical and chemical properties, such as large specific surface area, large adsorption capacity for pollutants and large number of active sites. Therefore, it is used widely in energy storage, sensors, superconducting materials and photocatalytic materials. Especially in photocatalytic materials, GO can capture photogenerated electrons, which can effectively improve the separation of photogenerated carriers, and increase the photocatalytic activity of semiconductors. Studies have shown that GO can significantly improve the photocatalytic activity of TiO_2, CdS, ZnO and Bi_2O_3. Although much research exists on GO and single semiconductor compounds, limited research exists on GO and binary heterojunction semiconductor composites. Hou et al. [17] synthesized Bi_2O_3/TiO_2/graphene composites, which can degrade Rhodamine B efficiently under visible light. Li et al. [18] synthesized CdS/RGO/TNTs photocatalytic materials by electrophoretic deposition (EPD) and successive ionic-layer adsorption and reaction (SILAR). They found that, compared with pure TNTs, RGO/TNTs and CdS/TNTs, CdS/RGO/TNTs have a higher photoelectrochemical (PEC) and photocatalytic (PC) activity. Our research group [15] synthesized a TiO_2/Bi_2WO_6 nanocomposite photocatalyst using a solvothermal method. The photocatalytic activity of the TiO_2/Bi_2WO_6 nanocomposites improved significantly. Compared with pure TiO_2 and Bi_2WO_6, TiO_2/Bi_2WO_6 exhibited significant enhancement in the degradation rate of ethylene. To further improve the photocatalytic activity of TiO_2/Bi_2WO_6 for ethylene degradation, in this study the TiO_2/Bi_2WO_6 nanoparticles are anchored to GO sheets to obtain $GO/TiO_2/Bi_2WO_6$ ternary composite photocatalyst by exploiting the large specific surface area and the effective built-in electric field of GO. Current studies in this area have not yet been reported in the literature.

In this study, a $GO/TiO_2/Bi_2WO_6$ ternary composite photocatalyst was prepared by adding GO during the solvent thermal synthesis of a TiO_2/Bi_2WO_6 heterojunction. X-ray diffractometry (XRD), Raman spectroscopy, scanning electron microscopy (SEM), X-ray photoelectron spectroscopy (XPS), ultraviolet (UV)-visible (vis) spectroscopy and photoluminescence spectroscopy (PL) were used to characterize the composite photocatalysts. The photocatalytic activity of ethylene degradation under visible light and stability of photocatalytic performance during recycling were evaluated. The mechanism of the enhancement in photocatalytic activity of the $GO/TiO_2/Bi_2WO_6$ composite is discussed.

2. Experimental section

2.1. Catalyst synthesis

All reagents were of analytical grade without further purification. Bi $(NO_3)_3 \cdot 5H_2O$ and $Na_2WO_6 \cdot 2H_2O$ were weighed at a 2:1 M ratio and dissolved in ethylene glycol under magnetic stirring to obtain liquids A and B. Polyvinylpyrrolidone (PVP K30, 0.75%) and GO dispersion (Produced by the XFNANO of China with the concentration of 2 mg/mL and sheet diameter less than 500 nm) were added into solution B, and were stirred magnetically to achieve sufficient dispersion. Liquid B was added dropwise to liquid A. Finally, 35% nano-TiO_2 (TiO_2 is a P25 powder manufactured by Evonik of Germany) was added to the mixture, to form a white suspension by magnetic stirring, and the pH was adjusted to 4. The suspension was placed in a 100-mL autoclave (using Teflon liner), kept for 15 h at 160 °C and then cooled down naturally to room temperature. The precipitate was removed from the reaction vessel, washed with distilled water, and then washed with anhydrous ethanol. The precipitate was dried in an oven at 80 °C, and then ground to obtain $GO/TiO_2/Bi_2WO_6$ composites. PVP K30 and TiO_2 were added as mass percentages of the Bi_2WO_6 precursor powder. The GO

dispersion was added at 0%, 0.25%, 0.5%, 0.75%, and 1.0% of the total mass of TiO_2/Bi_2WO_6 precursor powder and was recorded as TB, 0.25% GTB, 0.50% GTB, 0.75% GTB and 1.00% GTB, respectively.

2.2. Catalyst characterization

The crystal structure of the sample was probed with D8 ADVANCE X-ray diffractometry (XRD, Bruker, Germany). Samples were analyzed by LabRAM Aramis type Raman spectrometer (H.J.Y., France) with an excitation wavelength of 514.50 nm A Merlin field-emission scanning electron microscopy (Zeiss, Germany) was used to observe the morphology, particle size and dispersibility of the catalytic material. All samples were fixed on the sample stage and observed after sputtering with gold. Surface chemical composition of sample was investigated by ESCALAB 250 X-ray photoelectron spectroscopy (Thermo Fisher Scientific). The absorption spectra of the sample were analyzed using Lambda 950 UV–vis spectrophotometer (PerkinElmer, UK). Photoluminescence (PL) spectra of sample were recorded on RF-5130 fluorescence spectrophotometer (Shimadzu, Japan).

2.3. Photocatalytic activity evaluation

In order to evaluate the photocatalytic activity of GTB catalyst, GTB was loaded on an activated carbon fiber (ACF) membrane to study the ethylene degradation under visible light.

Photocatalytic film was prepared by dip coating method. Prepared GTB powder (2 g) was dispersed in 100 mL distilled water and 1% PVP K30 (based on GTB mass) was added. The suspension was stirred magnetically for 30 min and sonicated for 60 min. The circular ACF membrane (an area of 113 cm^2 and a thickness of 3 mm) was fixed on one end of the tensile tester, soaked into the suspension and pulled up at a rate of 4.2 mm/s. After coating, the materials were dried in a drying oven at 80 °C.

The photocatalytic degradation of the ethylene test platform used in this study is shown in Fig. 1. The platform consisted of a photocatalytic reaction system, a constant-temperature water-circulation system, and a gas chromatograph. The photocatalytic reaction system is composed mainly of an ultrahigh-pressure Xe lamp (light intensity 500 W), UV cutoff filter ($\lambda > 400$ nm), reaction film support, photocatalytic film (effective light area 226 cm^2), gas-circulation device, and photocatalytic reactor. Ethylene circulates around the reaction-film support through the gas-circulation device. A Xe lamp and UV cutoff filter provide visible light ($\lambda > 400$ nm) for the catalytic reaction. The constant-temperature water-circulation system can control the temperature of the entire reaction system to 20 ± 2 °C and the relative humidity was maintained between 20% and 30%. A gas chromatograph
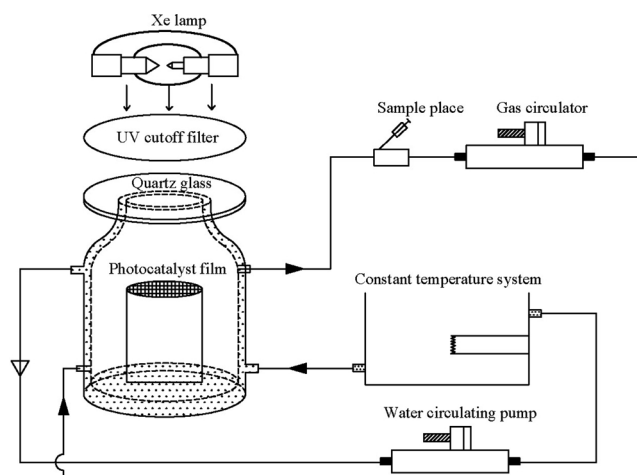

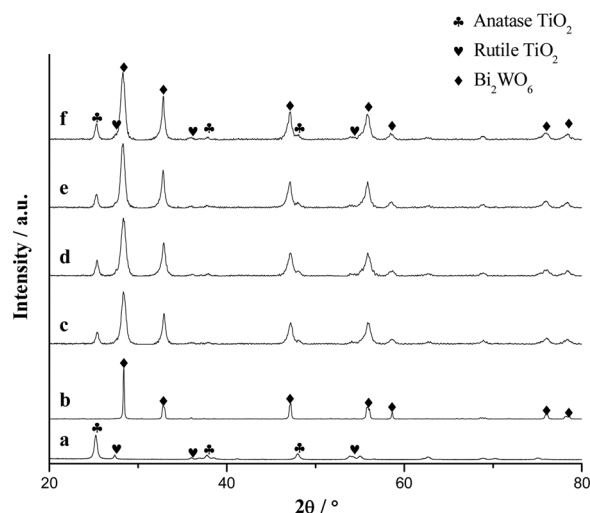**Fig. 1.** Photocatalytic degradation of ethylene test platform.

Fig. 2. XRD spectra. a. P25; b. Bi$_2$WO$_6$; c. 0.25% GTB; d. 0.50% GTB; e. 0.75% GTB; f. 1.00% GTB.

was used to determine the ethylene concentration in the reaction system.

The prepared ACF film was placed in a closed 2-L photocatalytic reactor at 20 ± 2 °C to conduct the visible-light catalytic degradation of ethylene. The ethylene test procedure was as follows. First, a volume of pure ethylene was injected into the photocatalytic reactor with a medical syringe. After 3 h, the adsorption of ethylene had reached equilibrium. The initial concentration of ethylene was determined by gas chromatograph. Then, constant-temperature water-circulation system was opened to maintain the reaction temperature at 20 ± 2 °C. Finally, the Xe lamp was turned on, and the ethylene concentration was measured every 30 min. Each sample was measured 8 times for a total of 240 min. And three parallel experiments were performed for each sample.

3. Results and discussion

3.1. XRD analysis

Fig. 2 shows the XRD spectra of the P25, Bi$_2$WO$_6$ and GTB composites with addition of different amount of GO. P25 is composed of anatase TiO$_2$ and rutile TiO$_2$. The crystal phase of Bi$_2$WO$_6$ belongs to orthorhombic. Compared with P25 and Bi$_2$WO$_6$, the GTB material is mainly composed of anatase TiO$_2$, rutile TiO$_2$ and orthorhombic Bi$_2$WO$_6$. No characteristic diffraction peak that belongs to GO is detected. The introduction of GO does not affect the crystal-phase structure of the TiO$_2$/Bi$_2$WO$_6$ material, possibly because the GO content in the composite is lower than the detection limit of the XRD [19]. The average grain size of each sample (131) is calculated by using the Scherrer formula (Table 1). As the amount of added GO increased, the average grain size of the GTB material decreased initially and then increased. When 0.75% GO was added, the sample had the smallest

Table 1
Average lattice size and lattice constant of GTB.

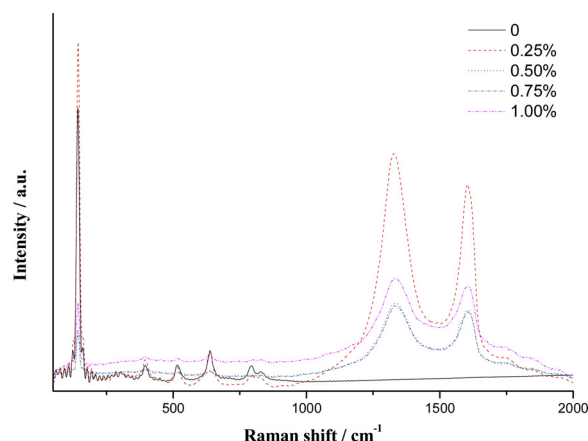| Sample	D/nm	Lattice constant		
		a/ Å	b/ Å	c/ Å
TB	26.0	5.45	16.34	5.44
0.25% GTB	16.8	5.45	16.45	5.43
0.50% GTB	17.9	5.46	16.33	5.44
0.75% GTB	14.6	5.44	16.41	5.46
1.00% GTB	19.0	5.45	16.37	5.45

Fig. 3. Raman spectra of GTB.

average grain size of 14.6 nm. The average grain size of the GTB was smaller than the average grain size of the TB, which indicates that an appropriate amount of GO addition can refine the average grain size of the GTB. The GO increases the barrier of intergranular diffusion and inhibits crystal growth [20].

3.2. Raman analysis

As shown in Fig. 3, typical vibrational bands of orthorhombic Bi$_2$WO$_6$ are observed at 260, 280, 305, 415, 717, 791 and 830 cm^{-1}. The typical vibrational bands at 141, 395, 515 and 633 cm^{-1} are attributed to TiO$_2$, and the strongest peak 141 cm^{-1} corresponds to the Eg mode [21]. The results show that the samples contain orthorhombic Bi$_2$WO$_6$ and TiO$_2$ are consistent with the XRD analysis results. New Raman shifts were found at 1325 and 1608 cm^{-1}. The Raman shift at 1325 cm^{-1} was found to be a D peak of GO, which is related to disordered carbon, edge carbon and defects. The Raman shift at 1608 cm^{-1} corresponds to the G peak of GO and is related to single-crystal and polycrystalline graphitized carbon [22]. The composite contains GO, but its content is low and it was not easily detected by XRD analysis. But the amount of GO added affected the Raman peak intensity of the Bi$_2$WO$_6$ and TiO$_2$ in the GTB samples. When the doping amount of GO is 0.75%, the characteristic Raman peak intensity of the Bi$_2$WO$_6$ and TiO$_2$ is the smallest.

The peak areas of D and G and the peak areas of G and Eg are calculated separately by integral calculation, and then the I_D/I_G ratio and I_G/I_{Eg} ratio are determined (Table 2). A smaller I_D/I_G ratio results in a more regular and complete GO honeycomb structure [23]. Table 2 shows that as the added amount of GO increases, the I_D/I_G ratio first decreases and then increases. The ratio is the smallest when the added amount of GO is 0.75%, which indicates that the GO structure in the sample is relatively complete. The intensity ratio between G band of GO and Eg mode of TiO$_2$ can indicate the increase or decrease of GO in GTB. As the amount of GO added increases, the I_G/I_{Eg} ratio also increases. Therefore, with the increase of GO content, the actual content of GO in the GTB also increases.

3.3. FE-SEM analysis

Fig. 4 shows FE-SEM images of GO and GTB samples. Fig. 4a shows

Table 2
I_D/I_G ratio and I_G/I_{Eg} ratio of GTB.

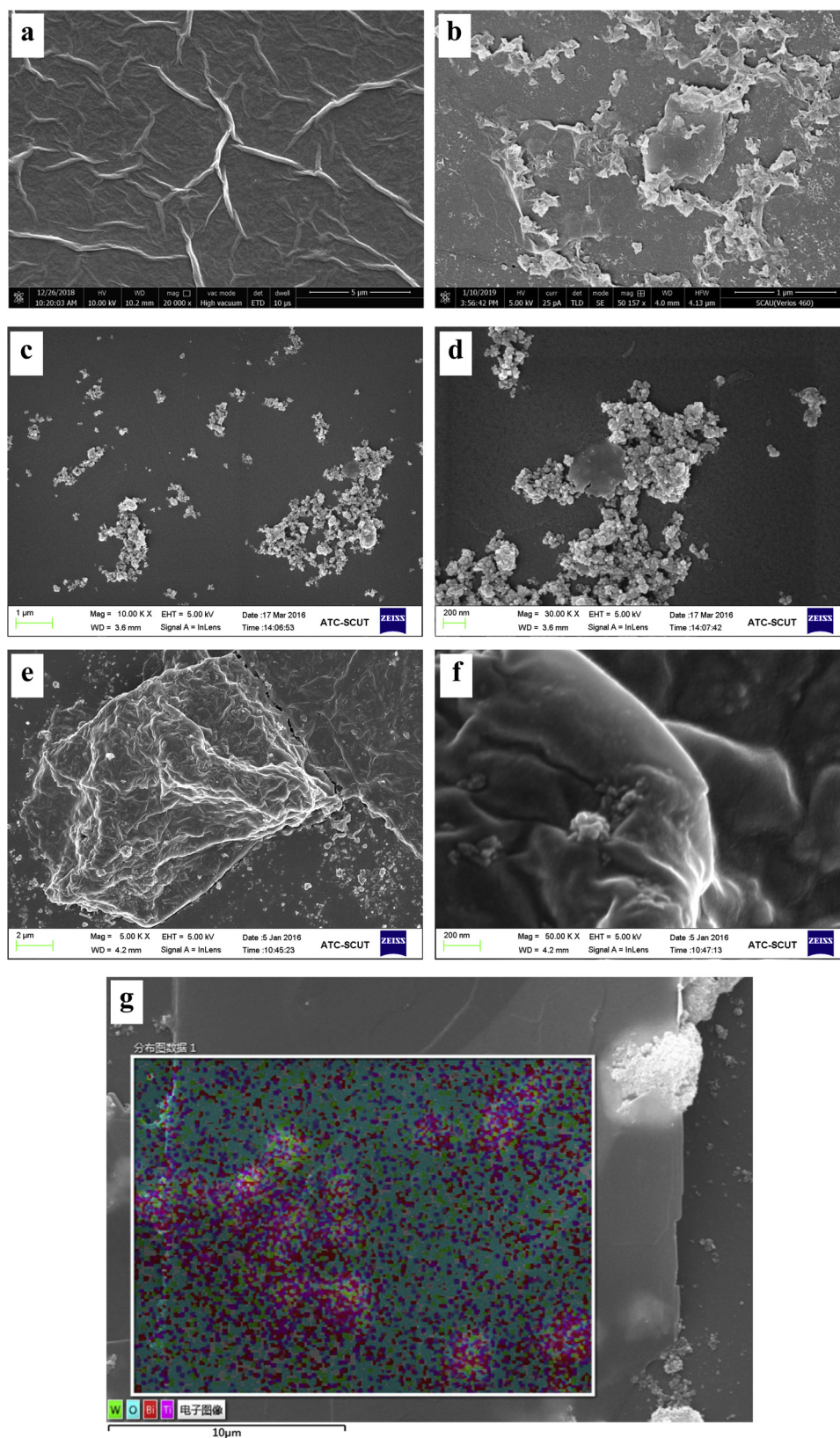| Sample	0.25% GTB	0.50% GTB	0.75% GTB	1.00% GTB
I_D/I_G ratio	1.39	1.31	1.29	1.34
I_G/I_{Eg} ratio	1.74	3.58	4.30	4.52

Fig. 4. FE-SEM images. a. GO before reaction; b. GO after reaction; c, d. 0.25% GTB; e, f. 0.75% GTB; g. 0.75% GTB's elemental mapping; h. 0.75% GTB's Bi mapping; i. 0.75% GTB's Ti mapping; j. 0.75% GTB's W mapping; k. 0.75% GTB's O mapping.

the FE-SEM image of GO before any treatment reaction. As can be seen from the figure, because the GO dispersion is not diluted, it shows a lot of layers of GO flake. Although GO flakes have some folds, there is no breakage or fragmentation in the whole area. Fig. 4b shows the FE-SEM

image of GO after 15 h at 160 °C reaction in a 100-mL autoclave (using Teflon liner). During the solvothermal reaction process, GO flakes break under the action of high temperature and high pressure, so the sizes of the GO flakes are different from one to another. When only 0.25% GO is
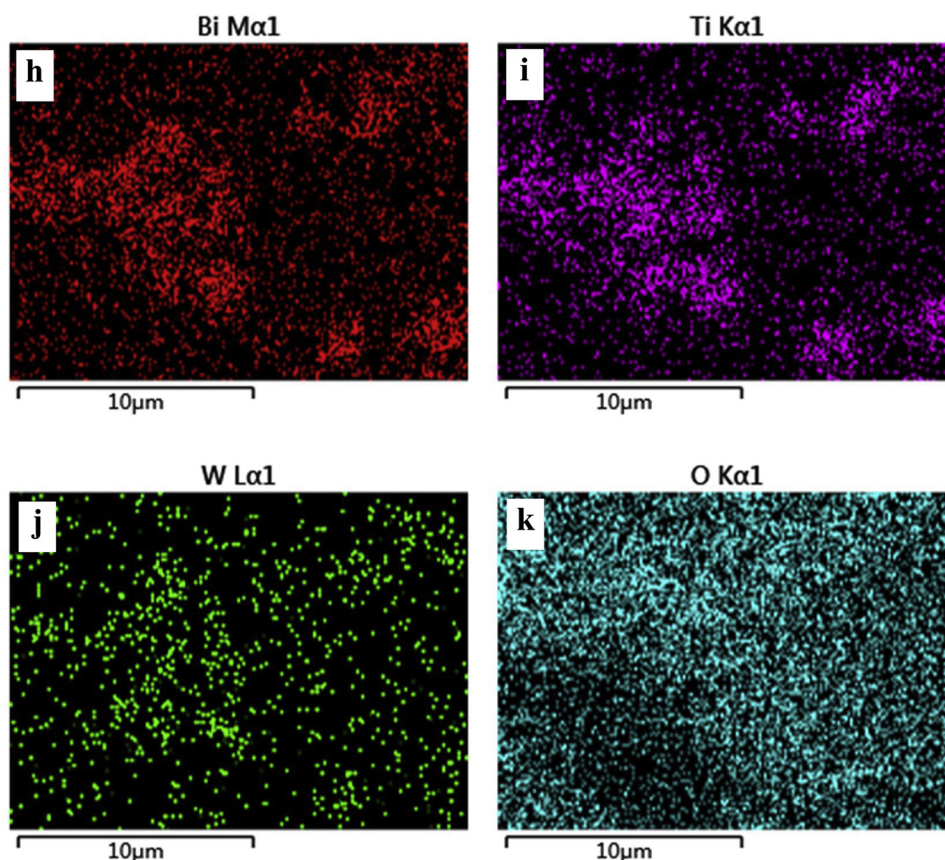
Fig. 4. (*continued*)

added, only a small piece of the GO covers the surface of the TiO_2/Bi_2WO_6 material because of insufficient GO addition. Most TiO_2/Bi_2WO_6 particles were present as agglomerates and failed to combine well with GO (see Fig. 4a, b). When the addition of GO is 0.75%, a more complete gauzelike GO is visible, and the TiO_2/Bi_2WO_6 particles are distributed on the GO surface (see Fig. 4c, d). Fig. 4e–j are SEM elemental mapping of the 0.75% GTB. From the graph, the distribution of Bi, W and Ti elements is approximately the same, which indicates that TiO_2 and Bi_2WO_6 are recombined and attach to the surface of GO. It is presumed that during GTB formation, as the surface of the GO is modified with a variety of polar oxygen-containing functional groups, titanium ions and bismuth ions can be bound easily to these active sites by hydrogen bonding and electrostatic adsorption, so that the formed TiO_2/Bi_2WO_6 attaches gradually to the GO surface. At the same time, the generated TiO_2/Bi_2WO_6 as a spacer can prevent interlamellar interactions and promote dispersion between GO sheets. This explains why there is no GO diffraction peak in the XRD spectra [24]. In the composite photocatalyst, GO interacts with TiO_2/Bi_2WO_6 to form an interfacial interaction, which benefits the transfer of a photogenerated charge at the interface. GO incorporation into TiO_2/Bi_2WO_6 results in a significant increase of the specific surface area and the number of photocatalytic active sites, which helps enhance the photocatalytic activity of the sample [25].

3.4. XPS analysis

Fig. 5a shows full XPS spectrum of the 0.75% GTB and GO. The 0.75% GTB sample contains mainly five elements of Bi, O, W, Ti and C. GO only contains two elements, C and O. We used the adventitious carbon (at 284.8 eV) as the standard for XPS peak correction.

Fig. 5b shows W4f spectrum. The electron binding energy of W4f appears at 35.5 eV and 37.6 eV which are attributed to the $W4f_{7/2}$ and $W4f_{5/2}$, respectively. Elemental W exists as W^{6+} in GTB sample [26].

Fig. 5c shows Bi4f spectrum. The electron binding energy of the Bi4f appears at 159.2 eV and 164.6 eV which are attributed to the $Bi4f_{7/2}$ and $Bi4f_{5/2}$, respectively [27]. Elemental Bi is present mainly as Bi^{3+} in the GTB sample, which is consistent with the results of Jia et al. [28].

Fig. 5d shows Ti2p spectrum. Ti2p has two peaks at 459.0 eV and 465.1 eV. These result from the spin-orbit splitting of Ti2p, and correspond to $Ti2p_{3/2}$ and $Ti2p_{1/2}$ in the anatase phase of TiO_2, respectively. These results indicate that Ti is present mainly as Ti^{4+} in the GTB sample [29]. $Ti2p_{3/2}$ and $Ti2p_{1/2}$ peaks are attributed to Ti−O−Bi and Ti−O−W, respectively.

Fig. 5e and f show C1s of spectrum 0.75% GTB and GO. The spectrum displays three peaks, ascribed to C−C bond (at 284.8 eV), C−O bond (at 286.6 eV), and C=O bond (at 288.7 eV). Compared to GO, the peak intensity of the oxygenated groups, especially that of C−O, on the 0.75% GTB decreased significantly, which indicates that GO is reduced partially during the reaction. But GO still has oxygenated groups, and TiO_2/Bi_2WO_6 can adhere to its surface through Ti−O bond.

3.5. UV–Vis analysis

Fig. 6 shows the absorption in the visible-light region is enhanced slightly in samples with 0.5% and 0.75% GO addition. This occurs because GO, as a blackbody material, has a light-absorbing property [30], which improves the absorption capacity of the sample for visible light. The steepness of the GTB spectrum indicates that its response to visible light results from energy-level transitions rather than from impurities that are introduced by GO addition.

The forbidden bandwidth of the GTB is calculated according to $Eg = \frac{1240}{\lambda}$, where Eg (eV) is the forbidden bandwidth of the sample and λ (nm) is the incident-light wavelength of the sample. The forbidden bandwidths of TiO_2, TB, 0.50% GTB and 0.75% GTB were 3.26 eV,
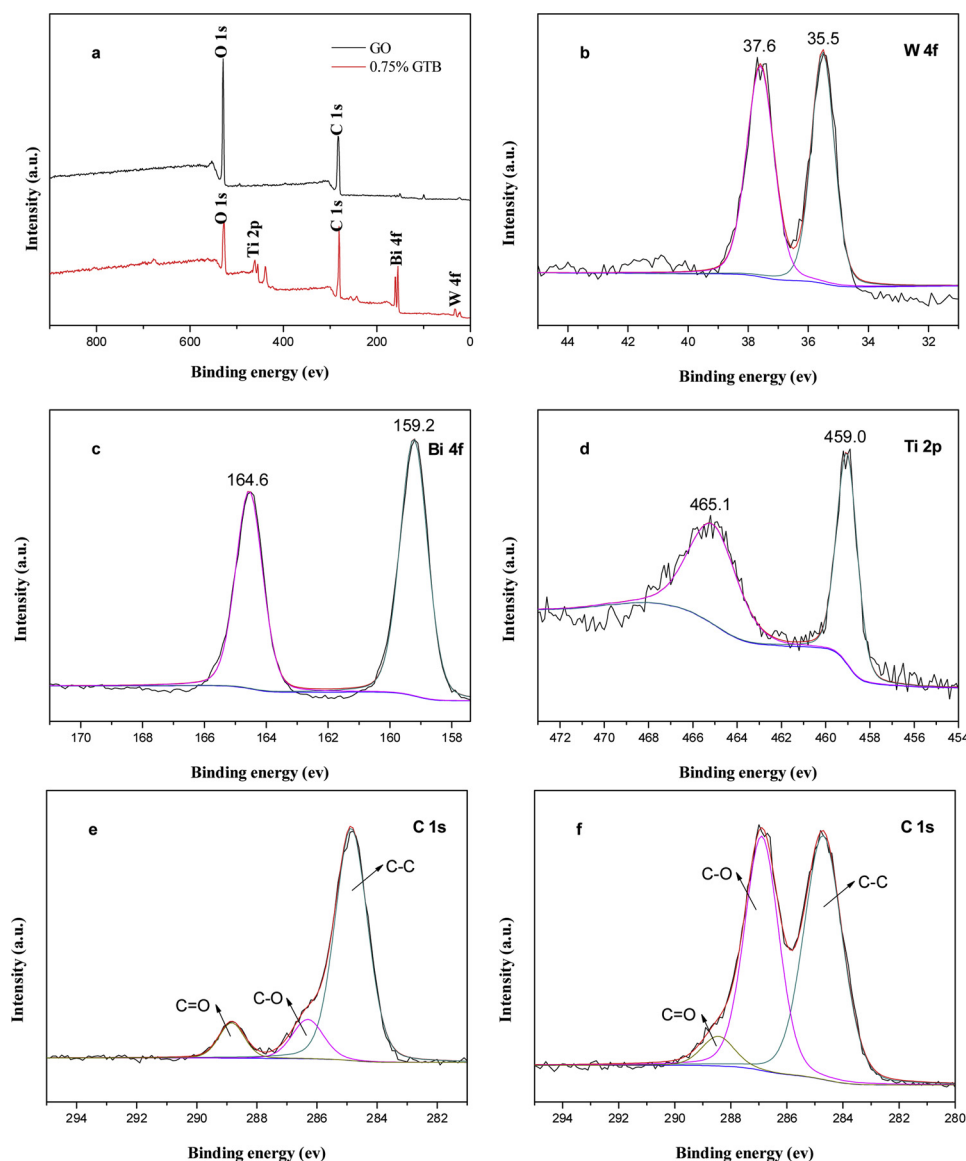
Fig. 5. XPS spectra. a. Full-spectrum graph; b. 0.75% GTB's W4f; c. 0.75% GTB's Bi4f; d. 0.75% GTB's Ti2p; e. 0.75% GTB's C1s; f. GO's C1s.
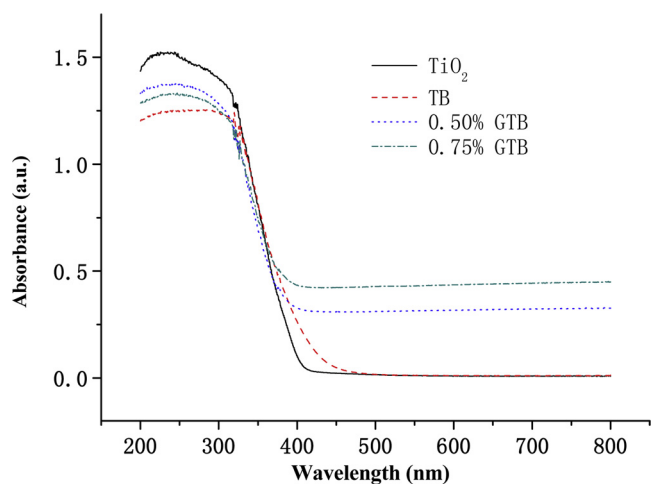

Fig. 6. UV–vis diffuse reflectance spectroscopy of GTB.

2.86 eV, 2.88 eV and 2.81 eV, respectively. Among them, the forbidden bandwidths of TB and 0.75% GTB are not much different, which

indicates that the loading of GO may increase the absorption of visible light. At the same time, GO has good conductivity due to partial reduction after solvothermal reaction. It can effectively promote separation and migration of photogenerated carriers, reduce the recombination rate [31]. And GO has a unique two-dimensional plane structure and conjugated large π bonds, which can adsorb the ethylene gas in a π-π conjugated form, thereby improving catalytic activity of GTB to degrade ethylene under visible light.

3.6. PL analysis

Photoluminescence (PL) spectra were used to analyze the migration, capture and recombination of photogenerated electron-hole pairs in the GTB multicomponent heterojunction catalysts. Fig. 7 shows that the photoluminescence spectra of the TB and GTB samples have similar shapes but different intensities. GO addition does not result in the appearance of new fluorescence phenomena. Therefore, the fluorescence effect of the TB samples originates from the formation of excitons, such as oxygen vacancies and defects on the nanoparticle surface [32]. With an increase in the amount of GO added, the intensity of the PL spectra showed an initial decreasing and then increasing trend. The order of the PL peak intensity of each sample was: TB > 0.25% GTB > 1.00%
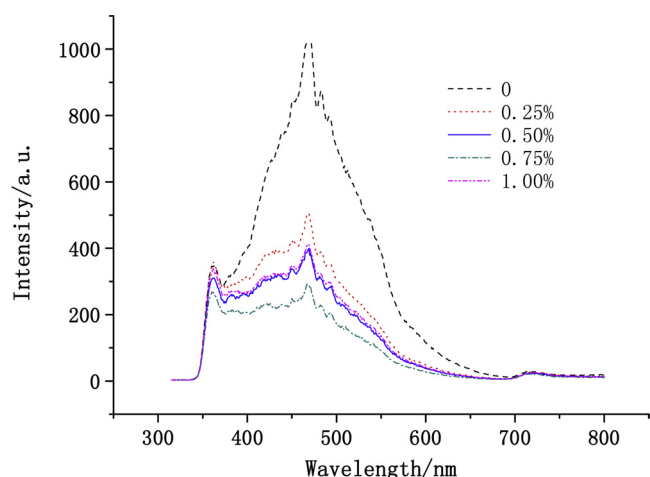
Fig. 7. Photoluminescence spectra of GTB.

Fig. 9. Ethylene degradation of different photocatalysts in 4 h of irradiation.

GTB > 0.50% GTB > 0.75% GTB. A lower PL peak intensity results in a lower recombination efficiency of photogenerated carriers [30]. From this, it can be confirmed that the addition of GO is the main reason for suppressing the photogenerated electron-hole pair recombination. High conductivity and electron-migration properties of GO also improved the visible-light response of GTB multi-heterojunction catalysts. The recombination of photogenerated electron-hole pairs was inhibited, which improved the visible-light catalytic activity.

3.7. Photocatalytic activity

The kinetics of photocatalytic degradation of ethylene were studied using the pseudo-first-order kinetics model [33]:

$$ln\frac{C_0}{C_t} = kKt = K't$$

where K' (min^{-1}) represents the apparent reaction rate constant, t (min) represents reaction time, C_t (mg/m^3) and C_0 (mg/m^3) represent the concentration of ethylene at time t = t and t = 0, respectively.

Fig. 8 shows that kinetics of ethylene degradation of GTB with different GO content under visible light irradiation. The correlation coefficients (R^2) of fitted line exceed 0.98, indicating that pseudo-first-order linear fitting has good correlation and can be used to study the ethylene degradation rate of composite catalysts. With an increase in the amount of GO added, the K' value increases initially and then decreases. When 0.75% GO is added, the K' value is the largest at
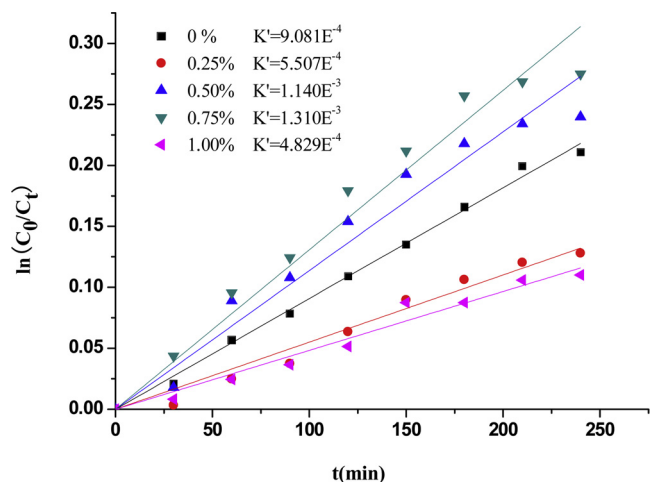
1.310×10^{-3} min^{-1}.

Fig. 9 shows the ethylene degradation of TiO$_2$, Bi$_2$WO$_6$, TB and GTB photocatalysts under visible light for 4 h irradiation. The degradation (%) of ethylene by pure TiO$_2$ and Bi$_2$WO$_6$ photocatalysts is significantly lower than that of the composite photocatalysts. With an increase in the amount of GO added, the degradation (%) of ethylene by GTB increased first and then decreased. The degradation (%) of ethylene by 0.75% GTB was highest at 24%, which was 5.7, 2.8 and 1.3 times that of pure TiO$_2$, Bi$_2$WO$_6$ and TB, respectively. Therefore, GO addition improves the photocatalytic activity of GTB composite photocatalysts significantly. This occurs because GO has a unique two-dimensional plane structure and conjugated large π bonds, which can adsorb ethylene gas on the surface as a π–π conjugate, which is beneficial to the photocatalytic reaction [34].

To investigate the stability of the photocatalytic activity for repeated use of GTB composite photocatalysts, 0.75% GTB samples were selected for four cycles of photocatalytic ethylene degradation experiments (see Fig. 10). The photocatalytic activity of the 0.75% GTB sample was reduced slightly after being recycled four times. The ethylene degradation (%) decreased gradually from an initial 24.0% to 22.6%, with an overall decrease of 6%. Therefore, the GTB composite photocatalyst had a good reusability and photocatalytic stability.

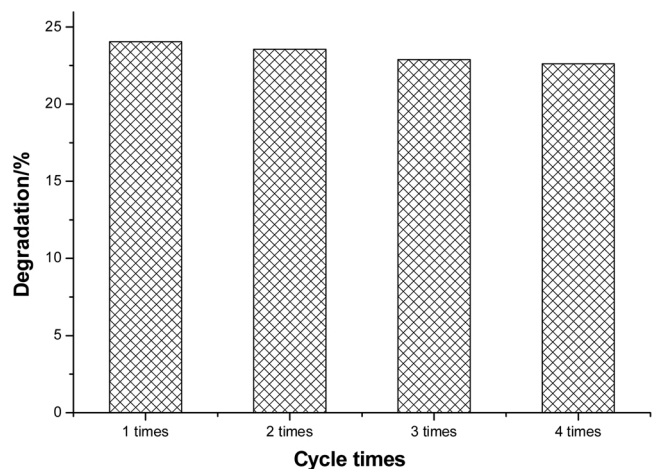**Fig. 8.** Kinetics of ethylene degradation over GTB under visible light irradiation.

Fig. 10. Photocatalytic degradation of ethylene using GTB: catalyst reuse studies.
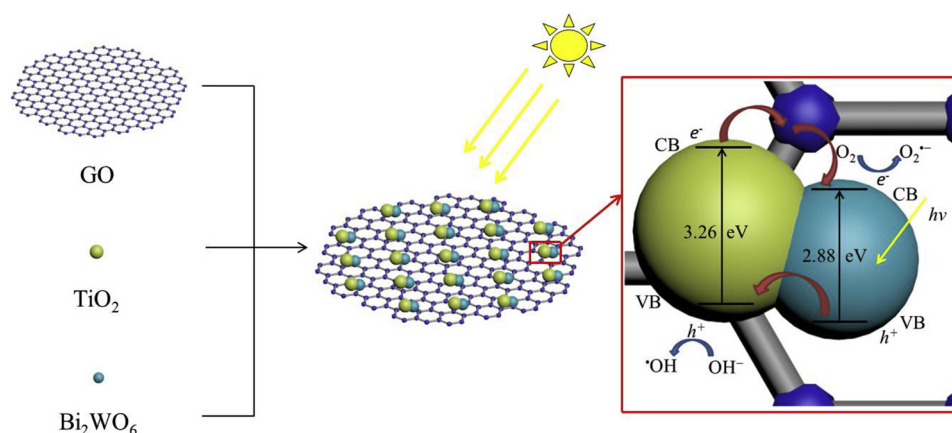
Fig. 11. Schematic diagram of photocatalytic enhancement mechanism by GTB.

3.8. Photocatalytic enhancement mechanism

On the basis of characterization results, photocatalytic enhancement mechanism of GTB is suggested as follows. GO addition causes O atoms in GO to replace O atoms in TiO_2 lattice to form Ti−O bonds and multiple heterojunctions with TiO_2 and Bi_2WO_6. Fig. 11 shows a schematic diagram of the band-energy structures of the GTB catalyst. The band gap of Bi_2WO_6 is 2.88 eV, and the band gap of TiO_2 is 3.26 eV. Because of energy band matching, the two can form a staggered heterojunction structure, which is consistent with related research results [35]. Under visible-light irradiation, Bi_2WO_6 and TiO_2 absorb photons and excite electrons (e^-) in valence band to conduction band, and photogenerated holes (h^+) are left in the valence band. Driven by thermodynamic electrochemical potential, the holes (h^+) in Bi_2WO_6 valence band migrate to the valence band of TiO_2, which effectively separates photogenerated electrons (e^-) and holes (h^+). The holes (h^+) in the valence band of TiO_2 can be captured by surface-adsorbed water or surface hydroxyls (OH^-) to generate hydroxyl radicals ($\cdot OH$). On the other hand, the electrons (e^-) on the conduction band migrate from the conduction band of TiO_2 to the conduction band of Bi_2WO_6 through GO transmission. The GO may be as an electron conductor accelerates the rate of electron migration and enhances the separation of electron-hole pairs [36,37]. At this point, electrons (e^-) that have migrated to the Bi_2WO_6 conduction band react with adsorbed oxygen on the surface of the GO to produce superoxide radical anions ($O_2^{\cdot-}$). $\cdot OH$ and $O_2^{\cdot-}$ can be used as strong oxidizers to oxidize ethylene to inorganic small molecules, such as CO_2 and H_2O. GO has a large specific surface area and a unique two-dimensional conjugated large π bond structure, which makes it highly adsorptive and able to adsorb a large number of ethylene molecules on its surface as π–π conjugates [38]. Because of its high conductivity and electron-transfer properties, the recombination of photogenerated electron-hole pairs is suppressed. Photogenerated charge carriers are separated, thus prolonging the lifetime of the photogenerated charge and providing more active free radicals to participate in the photocatalytic degradation of ethylene. Therefore, GTB exhibited a higher photocatalytic degradation than TB, and the addition of GO enhanced the visible-light catalytic activity of GTB.

4. Conclusions

A series of GTB composite photocatalysts were synthesized by a one-step solvothermal method combined with addition of dispersed GO nanosheets. The characterization of a GTB photocatalyst shows that the added GO can refine the average particle size of the GTB and result in a smaller grain size and lower crystallinity. The interaction of GO and TiO_2/Bi_2WO_6 produces an interfacial interaction and this combined with the large specific surface area of GO results in enhanced transfer of photogenerated charge, inhibition of the recombination of photogenerated electron-hole pairs, and increase in the number of photocatalytic active sites. XPS analysis shows that GO is reduced partially during the reaction and form multiple heterojunctions with TiO_2/Bi_2WO_6 by Ti−O bond. UV–vis analysis shows that the formation of multiple heterojunctions is conducive to reducing the forbidden bandwidth and improving the visible-light photocatalytic activity.

The GTB composite photocatalyst at optimum composition exhibits higher photocatalytic activity than its individual single or binary photocatalysts to degrade ethylene. When 0.75% GO is added, the highest visible-light catalytic activity is obtained, with the ethylene degradation (%) reaching 24%, which is 5.7 times, 2.8 times and 1.3 times that of pure TiO_2, Bi_2WO_6 and TB, respectively. Moreover, the GTB composite photocatalysis has good reusability.

References

[1] M. Liu, B.L. Gomes, I. Mila, E. Purgatto, L.E. Peres, P. Frasse, E. Maza, M. Zouine, J.P. Roustan, M. Bouzayen, J. Pirrello, Plant Physiol. 170 (2016) 1732–1744.
[2] Sandhya, Lwt-Food Sci. Technol. 62 (2015) 371.
[3] H. Einaga, J. Tokura, Y. Teraoka, K. Ito, Chem. Eng. J. 263 (2015) 325–335.
[4] S. Ye, J. Liang, X. Song, S. Luo, J. Liang, Biosyst. Eng. 150 (2016) 123–130.
[5] S. Ye, S. Zheng, X. Song, S. Luo, Appl. Surf. Sci. 341 (2015) 61–68.
[6] H. Yang, C. Ma, X. Zhang, Y. Li, J. Cheng, Z. Hao, ACS Catal. 8 (2018) 1248–1258.
[7] X. Liang, P. Wang, M. Li, Q. Zhang, Z. Wang, Y. Dai, X. Zhang, Y. Liu, M. Whangbo, B. Huang, Appl. Catal. B-Environ. 220 (2018) 356–361.
[8] H.H. Lin, A.Y. Lin, Water Res. 48 (2014) 559–568.
[9] W.W. Lai, Y. Chuang, A.Y. Lin, Environ. Sci. Pollut. R 24 (2017) 14595–14604.
[10] J. Low, S. Qiu, D. Xu, C. Jiang, B. Cheng, Appl. Surf. Sci. 434 (2018) 423–432.
[11] M. Park, B.S. Kwak, S.W. Jo, M. Kang, Energy Convers. Manage. 103 (2015) 431–438.
[12] X. Song, Y. Li, Z. Wei, S. Ye, D.D. Dionysiou, Chem. Eng. J. 314 (2017) 443–452.
[13] Y. Park, S. Lee, S.O. Kang, W. Choi, Chem. Commun. (Camb.) 46 (2010) 2477–2479.
[14] H. Zhang, X. Lv, Y. Li, Y. Wang, J. Li, ACS Nano 4 (2010) 380–386.
[15] X. Song, H. Wang, Y. Li, S. Ye, D.D. Dionysiou, Appl. Surf. Sci. 439 (2018) 815–822.
[16] F. Ma, Y. Yang, N. Li, Q. Yang, S. Li, L. Shen, Chin. J. Inorg. Chem 33 (2017) 1656–1666.
[17] J. Hou, C. Yang, Z. Wang, S. Jiao, H. Zhu, Appl. Catal. B-Environ. 129 (2013) 333–341.
[18] H. Li, Z. Xia, J. Chen, L. Lei, J. Xing, Appl. Catal. B-Environ. 168 (2015) 105–113.
[19] L.C. Sim, K.H. Leong, S. Ibrahim, P. Saravanan, J. Mater. Chem. A Mater. Energy Sustain. 2 (2014) 5315–5322.
[20] F. Zhang, S. Zhu, F. Xie, J. Zhang, Z. Meng, Sep. Purif. Technol. 113 (2013) 1–8.

[21] Y. Li, J. Liu, X. Huang, J. Yu, Dalton Trans. 39 (2010) 3420–3425.

[22] J. Yang, X. Wang, X. Zhao, J. Dai, S. Mo, J. Phys. Chem. C 119 (2015) 3068–3078.

[23] C. Chen, W. Cai, M. Long, B. Zhou, Y. Wu, D. Wu, Y. Feng, ACS Nano 4 (2010) 6425–6432.

[24] N. Thuy-Duong, H.P. Viet, E.W. Shin, P. Hai-Dinh, S. Kim, J.S. Chung, E.J. Kim, S.H. Hur, Chem. Eng. J. 170 (2011) 226–232.

[25] Y. Zhang, L. Fei, X. Jiang, C. Pan, Y. Wang, J. Am. Ceram. Soc. 94 (2011) 4157–4161.

[26] Y. Tian, L. Zhang, J. Zhang, J. Alloys. Compd. 537 (2012) 24–28.

[27] A.K.P. Mann, S.E. Skrabalak, Chem. Mater. 23 (2011) 1017–1022.

[28] Y. Jia, S. Zhan, S. Ma, Q. Zhou, Acs Appl. Mater. Inter. 8 (2016) 6841–6851.

[29] J. Tian, Y. Sang, G. Yu, H. Jiang, X. Mu, H. Liu, Adv. Mater. 25 (2013) 5075–5080.

[30] E. Gao, W. Wang, M. Shang, J. Xu, Phys. Chem. Chem. Phys. 13 (2011) 2887–2893.

[31] X. Zhang, S. Yu, Y. Liu, Q. Zhang, Y. Zhou, Appl. Surf. Sci. 396 (2017) 652–658.

[32] D. Wang, G. Xue, Y. Zhen, F. Fu, D. Li, J. Mater. Chem. 22 (2012) 4751–4758.

[33] Y. Lin, C. Weng, F. Chen, Chem. Eng. J. 248 (2014) 175–183.

[34] J. Low, J. Yu, Q. Li, B. Cheng, Phys. Chem. Chem. Phys. 16 (2014) 1111–1120.

[35] X. Sun, H. Zhang, J. Wei, Q. Yu, P. Yang, F. Zhang, Mat. Sci. Semicon Proc. 45 (2016) 51–56.

[36] A. Iwase, Y.H. Ng, Y. Ishiguro, A. Kudo, R. Amal, J. Am. Chem. Soc. 133 (2011) 11054–11057.

[37] X. Zeng, Z. Wang, N. Meng, D.T. McCarthy, A. Deletic, J. Pan, X. Zhang, Appl. Catal. B-Environ. 202 (2017) 33–41.

[38] S. Sun, W. Wang, L. Zhang, J. Xu, Appl. Catal. B-Environ. 125 (2012) 144–148.